Research Article

Aleksander Rodek*, Thilo Hahn, Jacek Kasprzak, Tomasz Kazimierczuk, Karol Nogajewski, Karolina Połczyńska, Kenji Watanabe, Takashi Taniguchi, Tilmann Kuhn, Paweł Machnikowski, Marek Potemski, Daniel Wigger, and Piotr Kossacki

Local field effects in ultrafast light-matter interaction measured by pump-probe spectroscopy of monolayer MoSe₂ (Supporting Information)

This document includes following content:

- 1. Co-circular simulations in the three-level system
- 2. Simulations in the ultrafast pulse limit
- 3. Impact of decay channels
- 4. Estimation of carrier concentrations
- 5. Determination of the pulse duration

1 Co-circular simulations in the three-level system

Figure 1(a) shows simulations for the co-circularly polarized excitation carried out in the three-level system (3LS). These are compared to cooresponding simulations in the two-level system (2LS) in Fig. 1(b), which are the same as in Fig. 4(b) in the main text. Regarding the spectral oscillations for negative delays and the energy shift and relaxation for positive delays, which are highlighted in Fig. 1(c), we find a good agreement. This shows that the experiment is well reproduced in both models. However, we find one slight difference in the 3LS compared to the 2LS: The amplitude of the signal recovers significantly slower for positive delays after it is quenched for $\tau \geq 0$. This leads to an overall better agreement with the experiment in Fig. 4(a) in the main text. The reason for this is that the decay rate in the 3LS is smaller than the effective one in the 2LS $\Gamma < \Gamma'$. Given that the scattering does not reduce the total occupation and that the EID depends on this total exciton occupation, the influence of the EID decays much slower in the 3LS. Therefore the signal recovery takes much longer in the 3LS.

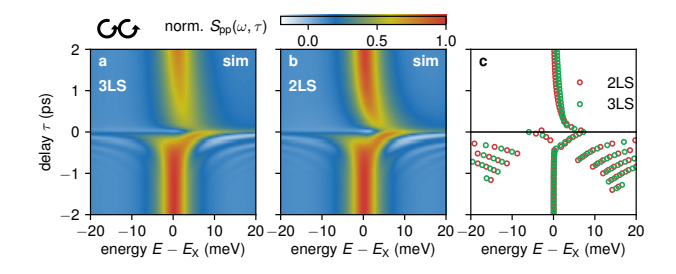


Fig. 1: Delay scan of simulated pump-probe spectra for cocircular polarization. (a) Simulation in the 3LS and (b) in the 2LS. (c) Local spectral maxima in the 2LS (red circles) and the 3LS (green circles).

To demonstrate that also the pump-probe spectra at $\tau=0$ in co-circular polarization can be well reproduced in the 2LS Fig. 2(a) shows the respective results. Panel (b) is the same as Fig. 5(a) in the main text. To reach the excellent agreement between simulation (bright) and measurement (dark) we determined the system parameters to $\Gamma'=1.6~{\rm ps^{-1}},~\beta=3~{\rm ps^{-1}},~{\rm and}~\hbar\theta_1^{(0)}^2V=\hbar\theta_1^{(0)}^2W=2.2~{\rm meV}.$ We again find that the effective decay rate has to be increased with respect to Γ in the 3LS to compensate for the missing inter-valley scattering channel. The energy

Physics, Faculty of Physics, University of Warsaw, 02-093 Warszawa, Poland, e-mail: aleksander.rodek@fuw.edu.pl **Thilo Hahn, Tilmann Kuhn,** Institut für Festkörpertheorie, Universität Münster, 48149 Münster, Germany, e-mail: t.hahn@wwu.de

Thilo Hahn, Paweł Machnikowski, Daniel Wigger, Department of Theoretical Physics, Wrocław University of Science and Technology, 50-370 Wrocław, Poland

Jacek Kasprzak, Université Grenoble Alpes, CNRS, Grenoble INP, Institut Néel, 38000 Grenoble, France

Kenji Watanabe, Takashi Taniguchi, National Institute for Materials Science, Tsukuba, Ibaraki 305-0044, Japan

Marek Potemski, Laboratoire National des Champs Magnétiques Intenses, CNRS-UGA-UPS-INSA-EMFL, 38042 Grenoble, France

^{*}Corresponding author: Aleksander Rodek, Jacek Kasprzak, Tomasz Kazimierczuk, Karol Nogajewski, Karolina Połczyńska, Marek Potemski, Piotr Kossacki, Institute of Experimental

shift as a function of the pump intensity is depicted in Fig. 2(c) and shows an excellent agreement between the 2LS, the 3LS simulations and the experiment.

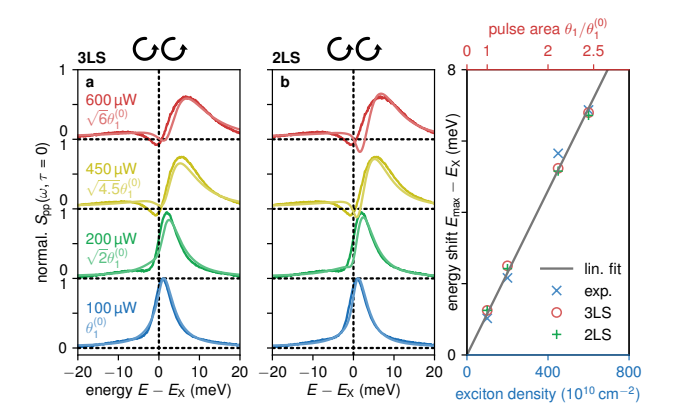


Fig. 2: Pump-probe spectra at pulse overlap. (a) Co-circular polarization with experiment in dark and simulation in the 3LS in bright colors. The smallest pulse area was determined to $\hbar\theta_1^{(0)}{}^2V=\hbar\theta_1^{(0)}{}^2W=2.2$ meV. (b) Same as (a) but in the 2LS (Fig. 5(a) in the main text). (c) Positions of the spectral maxima against the exciton density (bottom axis) in the experiment and the pulse area (top axis) in the simulation.

2 Simulations in the ultrafast pulse limit

In Fig. 3 we directly compare the numerically simulated spectra at pulse overlap, i.e., $\tau = 0$, in the 2LS with the ones from the analytical derivations. The solid lines stem from the numerical simulation and are the same as in Fig. 5(a) in the main text. The dashed lines are the respective results in the ultrafast pulse limit in Eq. (11) in the main text. In Fig. 3(a) we choose exactly the same parameters for the numerical and the analytical calculations. Overall we find that the spectral shapes agree very well for each considered pump pulse area. But we find that each spectrum in the delta-pulse limit shows a larger shift to higher energies. There are two reasons for this: (i) In the analytic result we entirely disregard the exciton decay $(\Gamma' = 0)$, which leads to a larger occupation and therefore a larger local field induced shift. (ii) During the excitation in the numerical calculation the system already dephases, which results in reduced polarization and occupation compared to the analytic result. This additionally results in an increased energy shift as explained before. To confirm this in the numerical simulations in Fig. 3(b) be set $\Gamma' = 0$ and

choose a renormalized pulse area to compensate for the dephasing during the pulse (see following section for more details). Now we indeed find an almost perfect agreement between the two sets of simulations. The remaining deviations stem from the still non-vanishing pulse durations of $\Delta t = 21$ fs in the numerical treatment. If this value is reduced to approximately 1 fs both simulations agree perfectly (not shown here).

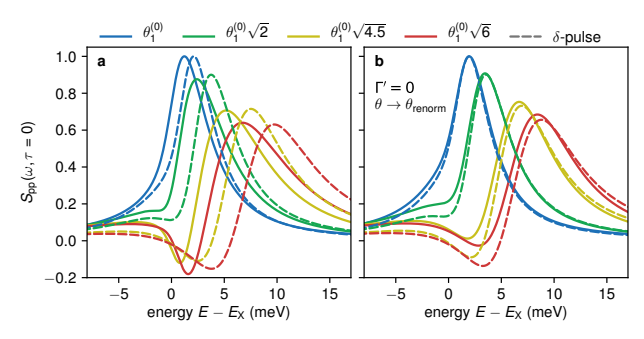


Fig. 3: Comparison of simulated spectra for vanishing delay $\tau=0$. (a) Numerical simulations for a pulse duration $\Delta t=21$ fs from Fig. 5(a) in the main text in sold. Corresponding analytical results from Eq. (11) in the main text. (b) Same as (a) but with $\Gamma'=0$ and renormalized pulse areas.

3 Impact of decay channels

As briefly discussed in the Theory section of the main text, the occupation after a single pulse depends on the considered system. As a reference we choose the pure 2LS without any decay excited with an ultrafast pulse where the occupation is given by $n = \sin^2(\theta/2)$, which is shown as black solid line in Fig. 4(a). When considering a non-vanishing pulse duration of $\Delta t = 21$ fs and adding the dephasing rate β and the effective decay rate Γ' from Fig. 5(a) in the main text we have additional contributions reducing the occupation after the pulse. This leads to the solid blue curve which clearly exhibits smaller occupations for a given pulse area. The occupation is further reduced when local field V and EID W from Fig. 5(a) are included in the red curve. Finally going to the 3LS by including the inter-valley scattering λ , and choose Γ from Fig. 5(b) (main text) instead of Γ' we get the green dashed curve with the smallest occupations. This discussion explains why we needed to choose smaller pulse areas in the 2LS than in the 3LS because be needed to reach approximately the same occupation in the different systems. It also shows why the simulations in the ultrafast pulse limit in Fig. 3

exhibit a larger energy shift because we chose the same pulse area as for the non-vanishing pulse duration.

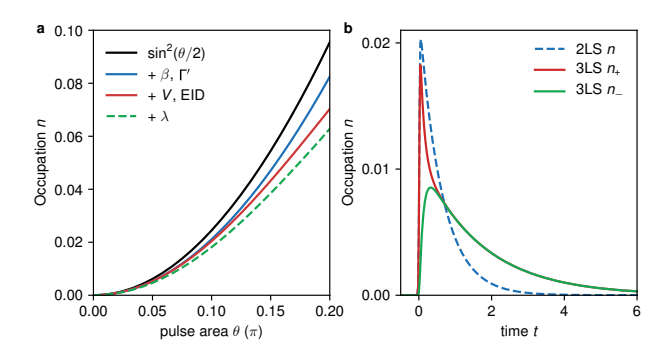


Fig. 4: (a) Pulse area dependence of the exciton occupation in the 2LS and 3LS model considering different contributions in the system dynamics. Black: pure 2LS in the ultrafast pulse limit, blue: including a non-vanishing pulse duration and dephasing rate β and effective decay rate Γ' , red: additionally including local field and EID, dashed green: adding inter-valley scattering int he 3LS. (b) Occupation decay after a pulse excitation in the 2LS (dashed blue) and the 3LS in red for n_+ and green for n_- .

To again embark on the interplay between the intervalley scattering λ and the decay rates $\Gamma^{(\prime)}$ in Fig. 4(b) we plot the occupation dynamics after a pulse excitation at t=0. The dashed blue curve depicts the 2LS with effective Γ' , while the solid red and green curve show n_+ and n_- in the 3LS, respectively. The laser pulse only addresses the $|+\rangle$ exciton in the 3LS, which after the excitation rapidly scatters into the $|-\rangle$ exciton. After the two occupations are balanced the decay slows down significantly. As explained in the Theory section of the main text the loss rate changes over time due to the scattering process. To compensate for this time dependence in the 2LS we choose the effective decay rate Γ' such that the mono-exponential decay is slower at the beginning and faster at the end of the relaxation as seen in Fig. 4(b).

Estimation of carrier concentrations

One of the consequences of the spatial separation of pump probe laser beams in the setup is the misalignment of the pump beam with the optical axis of the lens. This in turn results in a larger excitation spot on the sample, which on the one hand fully encompasses the probing area, but on the other hand makes it difficult to estimate the

actual density of photogenerated excitons. In order to calibrate the concentration of carriers during the pumpprobe measurement we measured the reflection from the sample with a single probing beam as a function of its power. The path of the probe laser beam lies on the optical axis of the lens allowing for good control over the size and shape of the laser spot on the surface of the sample. The final results presented in Fig. 5(c) show a pronounced blueshift of the exciton resonance that increases with the power of the laser. From this we can extract how it depends on the concentration. To do so we calculate the photogenerated carriers via $n = \gamma n_{\rm photon}/(\pi r^2)$, where γ is the total absorption of the ML, $n_{\rm photon} = PT/E_{\rm avg}$ is the number of photons per pulse with the laser power P, the laser repetition period T, the average energy of photons E_{avg} , and the laser spot radius r.

To calculate the absorption one needs to look at the overlap of the ML absorption coefficient and the fs pulse spectrum. In order to take into account contributions originating from light interfering between different layers of our sample we simulate the reflection by a transfer matrix method (TMM) similarly to previous works [1, 2]. In this approach the total reflection from the heterostructure is given by the ratio of transfer matrix elements R = $|M_{21}/M_{11}|^2$. Here, M is the product of all successive interface and layer matrices of the full heterostructure. The propagation of light on a single interface is given by

$$M_{\text{interface}}(n_1, n_2) = \frac{1}{2n_2} \begin{pmatrix} n_1 + n_2 & -n_1 + n_2 \\ -n_1 + n_2 & n_1 + n_2 \end{pmatrix}$$
(1)

where n_1 and n_2 are the refraction coefficients of neighboring materials 1 and 2. The propagation within a layer is described by

$$M_{\text{layer}} = \begin{pmatrix} e^{ikn_i d_i} & 1\\ 1 & e^{-ikn_i d_i} \end{pmatrix}$$
 (2)

where k is the wavevector in vacuum and n_i the refraction index and d_i the thickness of layer i.

In the simulation we use the following values for the refractive indexes of the heterostructure materials: $n_{\rm hBN}$ = 2.1, $n_{SiO_2} = 1.54$, $n_{Si} = 3.9$ [3–5]. In Fig. 5(a) we present the measured reflectance contrast from the heterostructure (blue) and the TMM simulation (red). The fitting was done via the resonance parameters included as an imaginary addition to the permittivity function of an isolated optical transition

$$\epsilon_{\rm Im} = k \frac{g}{(E - E_X)^2 + g^2} ,$$

where k is the amplitude, g the resonance width, and E_0 the resonance energy. The obtained resonance shape shown in Fig. 5(b) bares close resemblance to the imaginary susceptibility derived from a Kramers-Kronig transformation used in the main text. The absorption coefficient function

$$\alpha(\lambda) = \frac{4\pi\epsilon_{\rm Im}(\lambda)}{2n\lambda}$$

is then used in order to calculate the total absorption of our laser while considering its overlap with the resonance. Finally, $\gamma = (6.3 \pm 0.5)\%$ is used to calculate the density of photogenerated carriers in the reflection measurement. In Fig. 5(d) we show the exciton resonance as a function of carrier density. By fitting a linear function $\Delta E = \beta n$ to the data in the low excitation regime we retrieve $\beta =$ $(0.9 \pm 0.7) \times 10^{-12} \text{ meV cm}^2$ which is a value equivalent to what can be found in other works for similar MoSe₂ heterostructures and falls within an order of magnitude to a theoretical estimation of $\beta = 5 \times 10^{-12} \text{ meV cm}^2$ [1, 6]. Finally, by considering the blueshift in the pump-probe measurements we can translate the measured pumping power into the density of photogenerated excitons (see Fig. 5 in the main text). For the data presented in Fig. 5 an average pumping power of 100 μW corresponded to $n = 10^{12}/\text{cm}^2$.

5 Determination of the pulse duration

The temporal resolution of the pump-probe experiment is given by the laser duration, which we determine by an autocorrelation measurement. In order to take into account possible dispersion effects the probing point for the autocorrelation was chosen right before entering the cryostat after the beams have passed through all optical elements in the setup. The signal intensity is presented in Fig. 6 and fitted with a gaussian function of standard deviation $\Delta t_{\rm int} = 30$ fs. To retrieve the correct pulse duration for the electric field in Eq. (2) in the main text we have to scale fitted value for the intensity via

$$\Delta t = \frac{\Delta t_{\rm int}}{\sqrt{2}} \approx 21 \text{ fs}$$

and a corresponding full width at half maximum (FWHM) of $50~\mathrm{fs}.$

References

 G. Scuri, Y. Zhou, A. A. High, D. S. Wild, C. Shu, K. De Greve, L. A. Jauregui, T. Taniguchi, K. Watanabe,

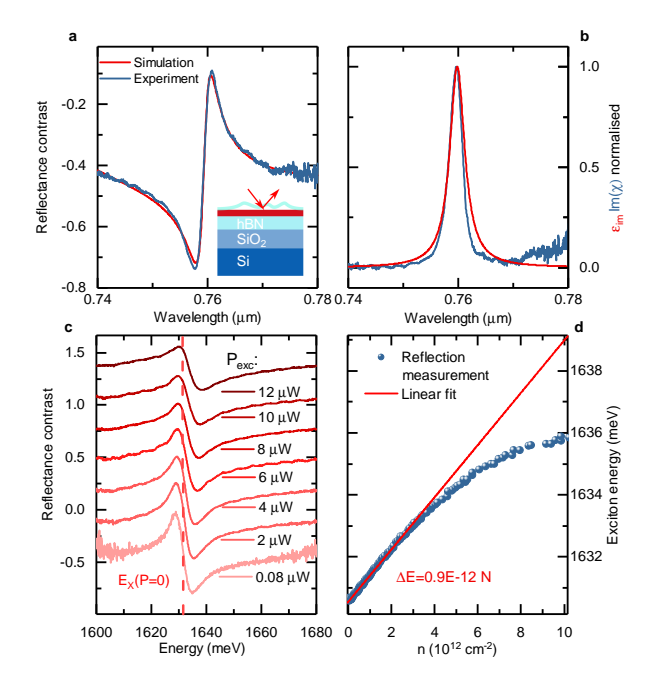


Fig. 5: (a) Reflectance contrast of the MoSe $_2$ monolayer and transfer-matrix method simulation. Simulation parameters: $d_{\rm SiO_2}=90$ nm, $d_{\rm bot}^{\rm hBN}=85$ nm, $d_{\rm top}^{\rm hBN}=30$ nm, $d_{\rm MoSe_2}=0.7$ nm, $d_{\rm air}=70$ nm, $n_{\rm hBN}=2.1$, $n_{\rm SiO_2}=1.54$, and $n_{\rm Si}=3.9$. Inset: Structure of the sample. (b) Normalized imaginary part of permittivity fitted from the TMM simulation and imaginary susceptibility extracted from the spectrum by the Kramers-Kronig transformation as mentioned in the main text. (c) Reflectance contrast of the sample measured for different powers of the fs laser. (d) Energy of neutral exciton resonance as a function of the density of photogenerated carriers.

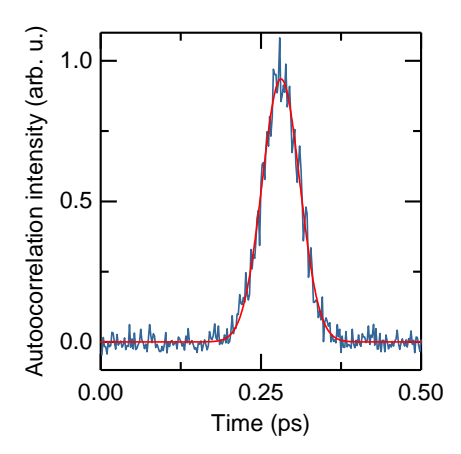


Fig. 6: Autocorrelation intensity of the laser beams used in the pump-probe experiments in blue and the fitted Gaussian in red.

P. Kim, M. D. Lukin, and H. Park. Large excitonic reflectivity of monolayer MoSe₂ encapsulated in hexagonal boron nitride. *Phys. Rev. Lett.*, 120:037402, 2018.

- [2] P. Back, S. Zeytinoglu, A. Ijaz, M. Kroner, and Atac Imamoğlu. Realization of an electrically tunable narrowbandwidth atomically thin mirror using monolayer $\mathsf{MoSe}_2.$ Phys. Rev. Lett., 120:037401, 2018.
- [3] S.-Y. Lee, T.-Y. Jeong, S. Jung, and K.-J. Yee. Refractive index dispersion of hexagonal boron nitride in the visible and near-infrared. Phys. Status Solidi B, 256(6):1800417, 2019.
- [4] I. H. Malitson. Interspecimen comparison of the refractive index of fused silica. J. Opt. Soc. Am., 55(10):1205-1209, 1965.
- [5] D. E. Aspnes and A. A. Studna. Dielectric functions and optical parameters of Si, Ge, GaP, GaAs, GaSb, InP, InAs, and InSb from 1.5 to 6.0 eV. Phys. Rev. B, 27:985-1009, 1983.
- [6] V. Shahnazaryan, I. Iorsh, I. A. Shelykh, and O. Kyriienko. Exciton-exciton interaction in transition-metal dichalcogenide monolayers. Phys. Rev. B, 96:115409, 2017.